Spatiotemporal characteristics of uniform momentum zones: Experiments and modeling

Angeliki Laskari, Charitha M. de Silva, Nicholas Hutchins, and Beverley J. McKeon

Phys. Rev. Fluids **7**, 104603 — Published 7 October 2022

DOI: 10.1103/PhysRevFluids.7.104603

Spatio-temporal characteristics of uniform momentum zones: experiments and modelling

Angeliki Laskari,[1,*] Charitha M. de Silva,[2] Nicholas Hutchins,[3] and Beverley J. McKeon[4]

[1] *Department of Process and Energy, Delft University of Technology, 2600 AA Delft, NL*
[2] *School of Mechanical and Manufacturing Engineering, University of New South Wales, Sydney, NSW 2052, Australia*
[3] *Department of Mechanical Engineering, University of Melbourne, Melbourne, VIC 3052, Australia*
[4] *Graduate Aerospace Laboratories, California Institute of Technology, Pasadena, CA 91125,USA*

(Dated: September 13, 2022)

The probability density function (p.d.f.) of the instantaneous streamwise velocity has consistently been used to extract information on the formation of uniform momentum zones (UMZs) in wall-bounded flows. Its temporal evolution has previously revealed patterns associated with the geometry and amplitude of the underlying velocity fluctuations [Laskari and McKeon, J. Fluid Mech. 913, A6 (2021)]. In this work, we examine the robustness of these patterns in a variety of datasets including experiments and wall-bounded flow models. Experimental datasets spanning a range of Reynolds numbers, with very long temporal and spatial domains, suggest that the rate of the observed temporal variations scales in inner units. The use of a convection velocity, uniform across heights, to transform space into time has a marginal effect on these features. Similarly, negligible effects are observed between internal and external geometries. Synthetic databases generated following the resolvent framework and the attached eddy model are employed to draw comparisons to the experimental databases. Our findings highlight the distinctive strengths of each: the broadband frequency input of the attached eddy model allows for a better statistical description as opposed to a narrow frequency input in the resolvent datasets; instantaneously, however, representative eddies are seen to lack some structural details leading to the observed temporal behaviour, which is better replicated by resolvent modes. Overall, given the considerable variety of the input data tested, the agreement between the datasets highlights the robustness of the spatio-temporal characteristics of the examined UMZs. It also underpins the need for their proper inclusion in UMZ modeling from a statistical as well as an instantaneous viewpoint; the current analysis accentuates important performance indicators for both.

I. INTRODUCTION

The undeniable importance of wall-bounded turbulence has led to intense research efforts on the topic during the past several decades, providing us with a wealth of available data (both numerical and experimental). Its complexity has stimulated the development of a wide range of models, seeking some level of simplification of these flows. Currently, given the sheer range of data and adopted modelling approaches, comparisons are not necessarily straightforward, especially when diverse models are involved; they are however crucial in improving flow models and their robustness as well as facilitating assessment of experimental data. In this work, we present a comparison between two current prominent modelling approaches—one equation based (resolvent framework [2]), and one conceptual (attached eddy model, AEM [3])—as well as between time-resolved and snapshot particle image velocimetry (PIV) data. The comparisons will be limited to the streamwise velocity component, and in particular the temporal characteristics of its instantaneous probability density function (p.d.f.), as described in [1]: the overarching aim is to evaluate the robustness of these features in a wide variety of data.

Since the work of Meinhart & Adrian [4], the p.d.f. of the instantaneous streamwise velocity has been increasingly scrutinised: local peaks in the p.d.f. have been shown to indicate the presence of large zones of uniform momentum (UMZ) in the flow [5], delineated by thin regions of intense shear [6, 7], reflected in the commonly observed staircase-like form of the instantaneous streamwise velocity profiles. From a structural perspective, these observations allowed connections with important notions of representative, energy-carrying, coherent structures populating the logarithmic and wake regions of wall-bounded flows [5], including large- and very-large-scale-motions (LSMs and VLSMs, respectively, [8–11]).

More recently, UMZ characteristics have also been explored through the lens of drag reduction strategies [12, 13]. In this context, a broad variety of input data has been employed to examine UMZs, including both experiments

* a.laskari@tudelft.nl

(PIV) and direct numerical simulations (DNS). Following the original experimental studies [4, 5], the presence and characteristics of UMZs (as well as the intense-shear interfaces separating them) have been analysed in experimental data of zero-pressure-gradient (ZPG), incompressible, smooth [1, 6, 7, 14–17] and rough [18] turbulent boundary layers (TBLs), TBLs subject to freestream turbulence [19], TBLs in adverse pressure gradient (APG) [20, 21], transonic, supersonic [20], and hypersonic [22] TBLs, in turbulent pipe flows [23], and atmospheric boundary layers [24, 25]. Collectively, these works highlight the robustness and importance of these flow features. Of these studies, the majority employed high spatial resolution databases to assess specific structural elements, while only a few have explicitly examined temporal characteristics, by employing stationary [1, 16, 20] and moving [17] time-resolved PIV. The main observations in this context, were an increased temporal persistence of high-speed structures in the log-region (involving a low number of UMZs [16]), as well as a presence of repeating patterns in the temporal evolution of the streamwise velocity p.d.f. [1, 17]. Recently, high resolution in both time and space domains has been available in DNS studies of ZPG and APG TBLs [26], as well as turbulent pipe flows [27, 28], however only a few studies (see [26]) explored the temporal persistence of UMZs specifically. They reported that high-speed structures are seen to persist for longer and are located closer to the freestream for ZPG flows, in line with experimental observations [16], while low-speed structures closer to the wall are more persistent in APG TBL flows [26]. One of the goals of this study is to explicitly assess the importance of temporal information for the resulting characteristics of the streamwise velocity p.d.f. and in particular the consequences of employing Taylor's hypothesis [29] for comparisons in the case of non-time-resolved datasets.

On the modelling side, there have been three distinct approaches that were specifically used to analyse UMZ development and characteristics, to date: the AEM [3], the resolvent framework [2] and the UMZ-vortical fissure model by Bautista *et al.* [30]. The first two were developed as conceptual and equation-based low-order flow representations, respectively. Their ability to reproduce key turbulent features and statistics guided subsequent fine-tuning [31] or input scale selection [32] during model development; resulting UMZ characteristics were then assessed as model outputs and compared with experimental observations. On the other hand, in the UMZ-vortical fissure model, the phenomenology of uniform momentum zones was used as model input while flow statistics were assessed as outputs in order to evaluate model performance [30]. Synthetic fields constructed using the AEM, were able to reproduce the mean number of UMZs and its experimentally observed logarithmic scaling with Reynolds number; the model also underlined essential trends in the resulting population density and vertical extent of the associated structures [14]. Using the resolvent framework formulation, streamwise velocity fields of a representative LSM were able to reproduce UMZ behaviour [15], while those composed of downstream travelling, single mode and multi-mode hierarchies in the log-region, could reproduce experimentally observed temporal patterns of the streamwise velocity p.d.f; the latter two also allowed clear associations of the p.d.f. behaviour with the underlying velocity fluctuations [1]. On the other end, starting with instantaneous streamwise velocity profiles composed of randomly displaced vortical fissures of concentrated vorticity (satisfying a mean momentum equation analysis), statistics up to third (skewness) and fourth order (kurtosis) from high Reynolds number DNS studies could be replicated particularly well [30]; the fissure's thickness was seen to decrease with friction Reynolds number and the velocity jump across each fissure to scale with the friction velocity. These key observations further motivated the refinement of a conceptual model by Chini *et al.* [33], based on large-Reynolds number asymptotic analysis of the Navier-Stokes (NS) equations, which describes a 3D self-sustaining-process (SSP) theory able to account for the formation and maintenance of UMZs with the aforementioned key attributes, in the inertial region of wall-bounded turbulent flows [34]. In this work, we focus on the first two approaches, namely the AEM and the resolvent framework; consistency of their background theoretical considerations has been previously examined [35], so here we are aiming to compare, for the first time, resulting flow representations and assess how well they match experimental observations. As mentioned above, the model output evaluated here is the p.d.f. of the streamwise velocity and in particular its temporal evolution; as such, and given that the approaches discussed here are designed to successfully replicate a very wide range of flow behaviours, model (and experimental) dataset comparisons herein are meant to be targeted and not necessarily indicative of general model performance or applicability.

In what follows, the experimental and modelling datasets used in this work will first be outlined. From a modelling perspective, the focus is entirely on structures anchored within the logarithmic region. Self-similarity imposes specific scaling relationships and allows for the most equitable comparison between the models (while the AEM contains exclusively self-similar eddies, the resolvent approach can include velocity modes throughout y—albeit with a higher degree of empiricism involved). The p.d.f. construction and analysis described in [1] will subsequently be briefly outlined and be expanded to account for the variety of input data employed in the present work. These tools will then allow comparisons of the p.d.f. behaviour between datasets in the results section, as well as some more in depth scrutiny of the previously observed patterns. Finally, some more in depth discussion and conclusions will follow.

II. DATASET DESCRIPTION

For the subsequent analysis, four different types of velocity fields are used: experimental velocity fields generated by time-resolved (TRPIV) and snapshot (SPIV) planar particle image velocimetry (PIV) and synthetic snapshots generated using the attached eddy model (AEM) and the resolvent framework (R). Both experimental and synthetic databases include datasets of internal (channel) and external (TBL) geometries and their details are provided in the sections below and outlined in table I. Coordinates x, y, and z are used to denote the streamwise, wall-normal, and spanwise directions, respectively and U, V, W the corresponding velocity components (lower case letters denoting fluctuations, following a Reynolds decomposition of the flow). Vectors are denoted with bold letters. Unless specified otherwise, all velocity components are in outer units, normalised using the freestream velocity, U_∞ (or centreline velocity U_{CL} for internal geometries).

TABLE I. Dataset details | $\mathcal{P}(U,t)$ construction details | symbol definition for each database.

Dataset	**Ref**	**Flow**	$\boldsymbol{Re_\tau}$	$\boldsymbol{L_x \times L_y}$	$\boldsymbol{dx^+}$	$\boldsymbol{dx^+|_{p.d.f.}}$	$\boldsymbol{dt^+|_{p.d.f.}}$	$\boldsymbol{\mathcal{P}_{th}}$	**Line**	**Marker**
SPIV1	[36]	TBL	2650	$11.6\delta \times 1.1\delta$	13	36	10.2	0.5	——	■
AEM	[31]	TBL	3200	$15.0\delta \times 1.3\delta$	32	32	9.7	0.5	-·-·-	▼
SPIV2	[39]	Channel	3900	$12.0\delta \times 1.0h$	29	29	10.1	0.5	——	■
SPIV3	[36]	TBL	5100	$11.9\delta \times 1.1\delta$	26	26	10.1	0.5	——	■
TRPIV	[16]	TBL	5300	$0.5\delta \times 1.2\delta$	27	27	10.4	0.5	- - -	□
R1	[1]	Channel	5300	$1.3h \times 1.0h$	27	27	10.4	3	·····	▽
SPIV4	[36]	TBL	7400	$11.6\delta \times 1.1\delta$	37	37	11	0.5	——	■
R2	[1]	Channel	15000	$0.5h \times 1.0h$	27	27	10.4	3	·····	▽

A. Time-resolved PIV (TRPIV)

The first experimental database contains a single dataset of time-resolved planar PIV data from a TBL at $Re_\tau = 5300$ in a streamwise–wall-normal plane [16]. The dataset comprises 37 time-resolved runs, each containing 10944 snapshots, covering about $14s$ of flow or 96 boundary layer turnover times (tU_∞/δ). Jones integral method was used to estimate δ, while u_τ was estimated employing the Clauser chart method [37] (similar results were obtained using the composite velocity profile by Chauhan *et al.* [38]). The field of view (FOV) is approximately $0.5\delta \times 1.8\delta$ in x and y, respectively. In order to minimize potential pixel-locking effects (especially pertaining to peak detection in the p.d.f. of the velocity), filtering in time (effective timestep of $dt = 0.027\delta/U_\infty$) and space (2D Gaussian filter with a 3×3 point kernel) was performed [14, 39]. More details on the experimental setup can be found in [16].

It should be noted here that—given the variety of the databases included in this study and our intent to assess the effects of using Taylor's hypothesis when comparing high- and low-speed data—we will consider this database as a baseline. It represents the full-scale problem when compared to the synthetic datasets and will not be modified when compared with the snapshot ones (all comparisons will be made in temporal units and as such only non-time-resolved data will be transformed by invoking Taylor's hypothesis).

B. Snapshot PIV - TBL (SPIV1, SPIV3, SPIV4)

A second planar PIV database of a TBL in streamwise–wall-normal planes, with an extended streamwise FOV ($L_x \approx 12\delta$), is also employed in this study. Details of the datasets can be found in de Silva *et al.* [36]. To summarise, the database includes three non-time resolved datasets, with 3000 independent velocity fields each, at three Reynolds numbers ($Re_\tau = 2650, 5100, 7400$). In order to maintain spatial resolution, while capturing a sufficiently large FOV to explore the large regions of coherence in the boundary layer a multi-camera arrangement is employed. Specifically, the experiments utilise an eight camera array aligned in the streamwise direction to capture a FOV spanning $\sim 12\delta \times 1.1\delta$ in x and y, respectively. Each camera provides a spatial resolution of 4008×2672 pixels. The corresponding spatial resolution for each dataset is summarised in table I. Illumination is provided a Big Sky Nd-YAG double pulse laser that delivers 120 mJ/pulse. An in-house code is used for processing the PIV image-pairs [40]. δ and u_τ are computed by applying the composite velocity profile of Chauhan *et al.* [38].

C. Snapshot PIV - Channel (SPIV2)

A third planar PIV database of a channel in streamwise–wall-normal planes, with an extended streamwise FOV ($L_x \approx 12\delta$), is also employed for completeness. Details of the dataset can be found in Kwon *et al.* [39]. To summarise, the database includes one non-time resolved dataset, with 590 independent velocity fields, at an intermediate Reynolds number of $Re_\tau = 3900$. In order to maintain spatial resolution (see table I), while capturing a sufficiently large FOV to explore the large regions of coherence in the boundary layer, a multi-camera arrangement is employed. Specifically, the experiments utilise a four camera array (each providing a spatial resolution of 4008×2672 pixels) aligned in the streamwise direction to capture a FOV spanning $\sim 12\delta \times 2h$ in x and y, respectively, although only the lower half of the channel was used in subsequent calculations.

D. Resolvent framework (R1, R2)

The synthetic database generated using the resolvent framework contains two datasets of turbulent channel flow at two different Reynolds numbers, henceforth referred to as R1 ($Re_\tau = 5300$) and R2 ($Re_\tau = 15000$). Each dataset contains 21 time-resolved runs, each containing 1300 snapshots of instantaneous streamwise velocity fields. Brief outlines of the resolvent framework and of the construction details of these snapshots are included here for completeness; for more details the reader is referred to [41] and [1], respectively.

The resolvent framework formulation for wall bounded flows [2], treats the NS equations as an input-output system: the non-linear term $\boldsymbol{f_k}$, acts as an intrinsic forcing, exciting the linear NS operator (the resolvent) $\boldsymbol{\mathcal{H}_k}$, following a Fourier transform in the homogeneous directions in space and in time, with $\boldsymbol{k} = (k_x, k_z, \omega)$ denoting the wavenumber/frequency triplet. The corresponding output response from this forcing, $\boldsymbol{u_k}$, comprises downstream propagating travelling waves and represents, in the Fourier domain, the velocity fluctuations around a wall-varying mean profile $U(y)$, based on a Reynolds decomposition of the flow. The linear operator requires only knowledge of $U(y)$ for its construction and, following a singular value decomposition, can be formulated in terms of left ($\psi_{\boldsymbol{k},j}$) and right ($\phi^*_{\boldsymbol{k},j}$) singular functions and singular values ($\sigma_{\boldsymbol{k},j}$) for each $\boldsymbol{k}$:

$$\mathcal{H}_{\boldsymbol{k}} = \sum_{j=1}^{\infty} \psi_{\boldsymbol{k},j} \sigma_{\boldsymbol{k},j} \phi^*_{\boldsymbol{k},j}. \tag{1}$$

The velocity response can then be approximated as a weighted sum of resolvent modes [41]:

$$\boldsymbol{u_k} = \sum_{j=1}^{\infty} \sigma_{\boldsymbol{k},j} \psi_{\boldsymbol{k},j} \overline{\chi}_{\boldsymbol{k},j} = \sum_{j=1}^{\infty} \psi_{\boldsymbol{k},j} \chi_{\boldsymbol{k},j}, \tag{2}$$

where the weights $\overline{\chi}_{\boldsymbol{k},j}$ are the coefficients of projection of the true non-linear forcing $\boldsymbol{f_k}$ onto the forcing modes, and $\chi_{\boldsymbol{k},j} = \sigma_{\boldsymbol{k},j}\overline{\chi}_{\boldsymbol{k},j}$. The resolvent operator has been shown to be low rank for those wavenumber triplets corresponding to important features of wall-bounded turbulence [41] and in what follows a rank-1 approximation will be adopted and the singular value subscript j will be dropped for clarity: $\boldsymbol{u_k} = \psi_{\boldsymbol{k}} \chi_{\boldsymbol{k}}$.

In order to construct the datasets discussed above, an appropriate selection of key wavenumber triplets is required; for each resulting response mode, the corresponding projection weight $\chi_{\boldsymbol{k}}$ is subsequently chosen and the full fluctuating velocity contribution is then superimposed on the known mean profile. For the two datasets included here, the discrete wavenumber/frequency input selection is guided on one hand by the need to include representative log region structures while allowing enough complexity to break the purely periodic nature of the model, and on the other by a wish to retain as much simplicity as possible. Given those constraints, the datasets are constructed using three self-similar hierarchies, localised in the log region and comprising five (six) triadically consistent members each, in the case of R1 (R2). With respect to the modes' wall-normal location, the shortest member of each hierarchy is centred at the start of the inertial region in the mean velocity profile, $y_{c,5}/h = 3/\sqrt{Re_\tau} = 0.0046$ ($y_{c,6}/h = 0.0245$) [42], and defines the location of all other members in the hierarchy through: $y_{c,m} = A^{5-m} y_{c,5}$ ($y_{c,m} = A^{6-m} y_{c,6}$) for R1 (R2). The longest member in each hierarchy is constrained by $y_{c,1}/h \leq 0.4$, thus prescribing the total number of members, while A is chosen equal to the golden ratio, $\phi = 1.6$. With respect to the modes' wavenumber content, we select the wavelength of the largest mode in one of the hierarchies to be representative of an LSM, with $k_{x1} = 1.8$ ($k_{x1} = 2$) for R1 (R2). Its corresponding spanwise wavenumber k_{z1}, is chosen such that, given the scaling relationships $\lambda_z \sim y_c$ and $\lambda_x \sim y_c^2$, the aspect ratio condition ($\gamma = k_z/k_x \gg 1$) is satisfied throughout the rest of the hierarchy [43]. The wavenumbers of the outmost modes in the other two hierarchies are selected to be triadically consistent, while being non-integer multiples of each other; geometric self-similarity then dictates the wavenumbers for the rest of the modes

and their convection velocity is prescribed by their wall normal location: $c_m = \overline{U}(y_{c,m})$. Finally, given the choice of wavenumber/frequency triplets, the projection weights for the resulting response modes are selected separately and chosen such that the resulting fluctuation intensity ($u^2_{\boldsymbol{k}}$) decreases logarithmically with y.

E. Attached Eddy Model (AEM)

A synthetic dataset generated following the AEM is included in the analysis. The database is set up following the configuration published in Eich *et al.* [31]. To summarise, the AEM flow fields are computed based on a packet of Λ eddies, which has been shown to both statistically [44] and structurally represent a turbulent boundary layer [14]. A set of vortex rods that contain a Gaussian distribution of vorticity about its core are used to construct the representative eddies. To compute the flow field, Biot-Savart calculations are performed over the vortex rods. This process is then repeated for each hierarchy of representative eddies in the field, here chosen to be six, which corresponds to a flow field at $Re_\tau = 3200$. The domain size was chosen such the maximum of the Reynolds shear stress is one and $\kappa \approx 0.4$ [14].

III. PDF CONSTRUCTION

The p.d.f. of the streamwise velocity, $\mathcal{P}(U)$, is constructed using instantaneous velocity vectors from either consecutive snapshots within time-resolved runs (TRPIV, R1, R2, figure 1b) or from spatially overlapping regions of independent, non-time resolved snapshots (SPIV1, SPIV2, SPIV3, SPIV4, AEM, figure 1a). For the latter, the long streamwise extent available allows the snapshots to be divided in equidistant regions, for each of which a p.d.f. is computed (solid black outlines and sharp contours in figure 1a). Spatial (and temporal) coherence is then provided by the p.d.f.s of consecutive overlapping regions in x (dashed outlines in figure 1a) with increasing x indicating previous time instances. This overlap is chosen such that, assuming a single, uniform convection velocity, the resulting temporal resolution of the p.d.f.s is comparable between the snapshot and time-resolved datasets. It should be noted here that, temporal resolution is matched in inner units ($dt^+|_{p.d.f.}$ in table I) which allows for a better scaling analysis for the range of Reynolds numbers included, making this the only difference from the analysis described in [1]. This is further ensured by the choice of convection velocity used to transform space to time ($U_c = 0.81U_\infty$), primarily chosen to correspond to the convection of a representative large-scale structure (see for example [45]). One of the goals of the present study is to identify to which extent such an assumption affects the resulting p.d.f. behaviour. For the AEM, it should also be noted that employing a wall-normal varying convection velocity (and periodic boundary conditions), as well as incorporating spanwise meandering, as described in Eich *et al.* [31], only led to marginal changes in the metrics presented here, while the overall trends remained the same. Constraints for the construction of the p.d.f. are imposed in both x and y, in all datasets. With respect to x, the streamwise extent used to construct the p.d.f. is chosen such that the observed modal peaks in the p.d.f. are well-converged, without averaging out of the smallest modal peaks present in each frame. Following [14], an optimal streamwise extent of $\mathcal{L}^+_x|_{p.d.f.} = 2000$, is chosen for all datasets. In the wall-normal direction, all velocity vectors within the turbulent region are included; we only exclude those belonging in the irrotational freestream (quiescent core) in external (internal) geometries. For consistency and simplicity, the turbulent/non-turbulent interface is identified using the iso-contour lines of $U = 0.95U_\infty$ for all datasets, following [39]. We note that the use of other methods such as a kinetic energy threshold [46] for the two experimental databases did not alter any of the results or conclusions presented herein. It did however, afford, a smoother freestream identification for the TRPIV dataset compared to the abrupt drop of the high p.d.f. values seen here (figures 2 and 6a), likely due to increased freestream turbulence levels present in that flow (see also the relevant discussion in [16]). Similar to the temporal resolution requirements discussed above, comparable spatial resolution (in wall-units) for the p.d.f. construction is also ensured between datasets ($dx^+|_{p.d.f.}$ in table I), by under-sampling the lower Reynolds number ones. The vectors contained within these limits are then distributed in 67 bins for $U \in [0, U_\infty]$ (of size approximately $0.4 \pm 0.04U_\tau$).

The resulting $\mathcal{P}(U,t)$ reveal interesting visual differences depending on the chosen scaling, the Reynolds number of each dataset, as well as the dataset type (experimental or synthetic). Regarding experimental datasets, the use of a uniform convection velocity does not seem to affect the resulting p.d.f. patterns, while the temporal dataset (TRPIV) is seen to result in slightly more noisy fields (figure 2). It should be noted here that, these temporal patterns in $\mathcal{P}(U,t)$, are discussed on the basis of variations in $U_*(t)$: $U_* = \min(U|\mathcal{P}(U,t) > \mathcal{P}_{th})$ (see figure 3), following the procedure proposed in [1]. We are particularly interested in the temporal rate of transitions in U_*, defined as the angle: $\phi = \tan^{-1}(\Delta U_*/\Delta t)$. The threshold $\mathcal{P}_{th}$ used for each of the datasets can be found in table I and for further details on how that choice influences the analysis, the reader is referred to the relevant discussion in [1]. Returning to the dataset comparison (figure 2), the above defined rate of transitions is seen to increase with Reynolds number

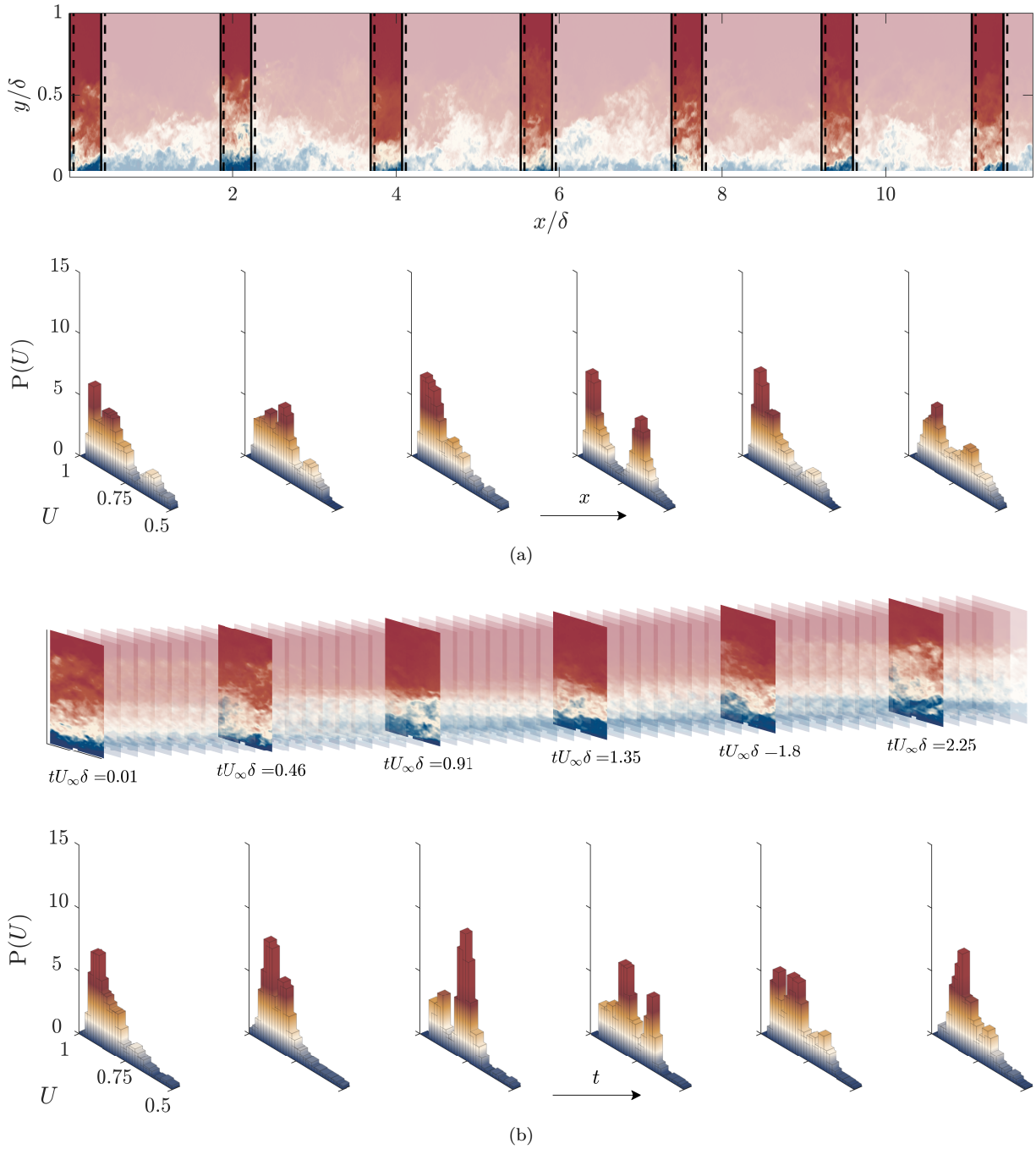

FIG. 1. Construction of $\mathcal{P}(U,t)$: (a) Spatial Data (SPIV1, SPIV2, SPIV3, SPIV4, AEM), (b) Temporal Data (TRPIV, R1, R2). In (a) the full spatial extent, L_x, is divided into regions of $\mathcal{L}_x^+|_{p.d.f.} = 2000$, while the same extent is selected from the time-resolved snapshots in (b). In order to match the temporal resolution in (b), an appropriate level of spatial overlap is used for each consecutive region in (a) (indicated with dashed lines), when constructing the p.d.f., while also assuming a constant $U_c = 0.81$.

when scaled in outer units, while better agreement is observed when the temporal extent is matched in wall units. With respect to the dataset type, and before moving forward with a quantitative analysis of these features, from a purely visual inspection, the two synthetic databases are able to reconstruct different aspects of the experimental patterns. The AEM dataset, given its broadband frequency input, allows some level of variation in $\mathcal{P}(U,t)$ for a larger range of velocities, compared to the resolvent framework datasets which contain a pre-selected set of scales (particularly notable for velocities $< 0.6U_\infty$). However, the largest $\mathcal{P}(U,t)$ values are confined to a very narrow range

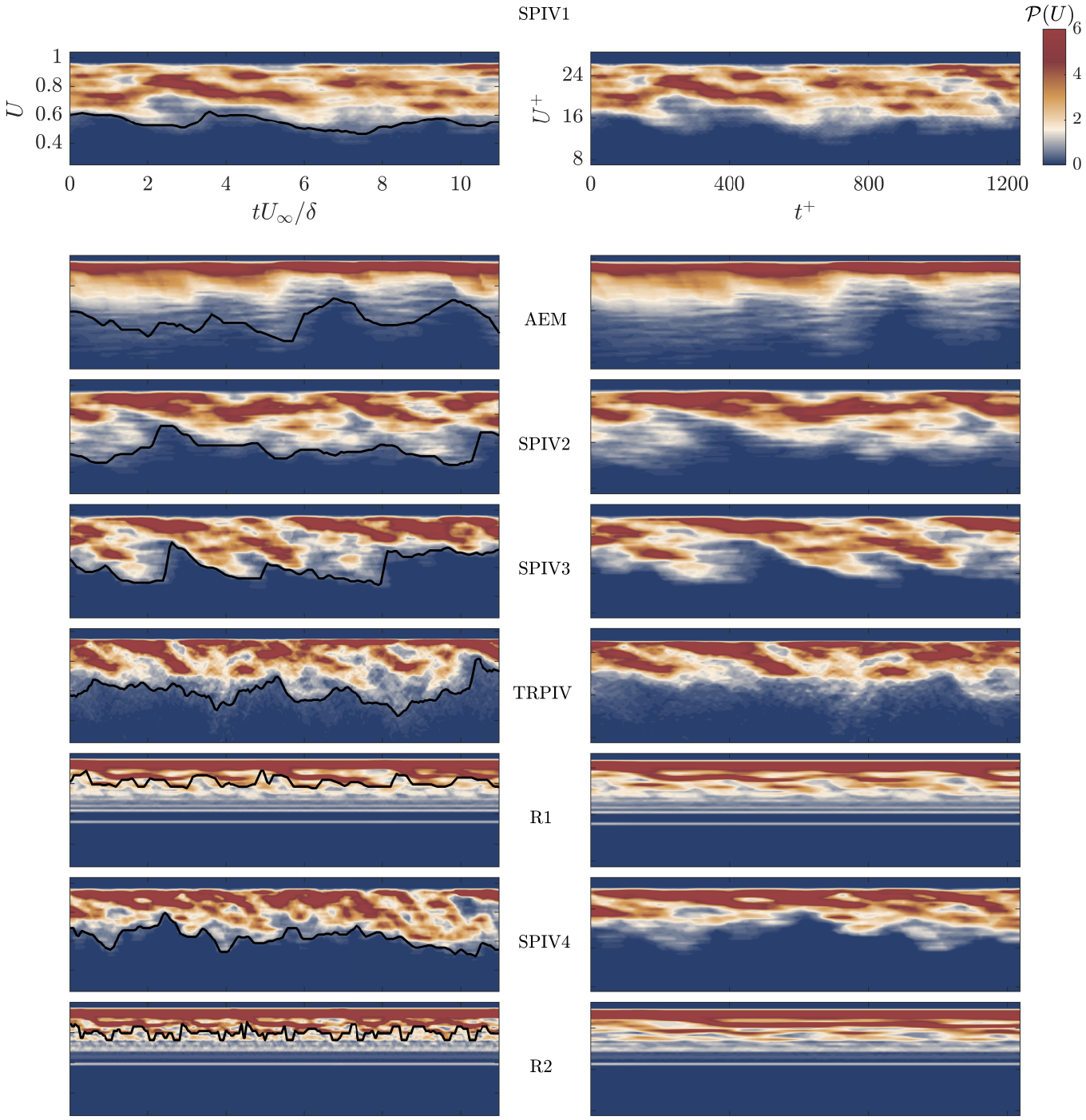

FIG. 2. Variation of $\mathcal{P}(U)$ over time in increasing Re_τ from top to bottom. Matching temporal extent in outer (left) and inner (right) units. Black solid lines denote $U_* = \min(U|\mathcal{P}(U,t) > \mathcal{P}_{th}$.

around $0.95U_\infty$ for the AEM and although some transitions to lower velocities are still observable and comparable in rate with the experimental datasets, they are much less discernible. In contrast, the patterns from the two resolvent datasets are more clearly formed and are also seen to qualitatively support the aforementioned Reynolds number variation in terms of their temporal extent. These differences between the models, which will be analysed in more detail in the next sections, essentially reflect the relative lack of frequency content for the chosen resolvent datasets and an incomplete instantaneous spatial/temporal organisation for the AEM.

In the quantitative analysis that follows, statistics of the angles ϕ describing the transitions in $\mathcal{P}(U,t)$, are compared

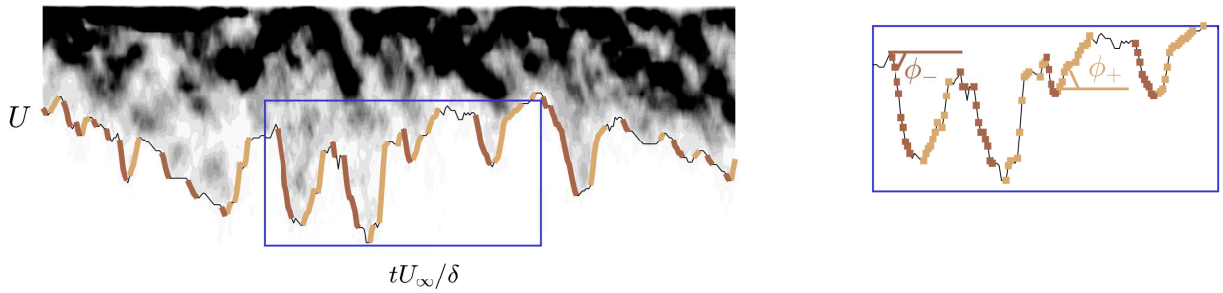

FIG. 3. An illustration of the transitions in $\mathcal{P}(U,t)$ - TRPIV, adapted from [1]. The identified ϕ_+ ($\Delta U_* > 0$, light colours) and ϕ_- ($\Delta U_* < 0$, dark colours) transitions of U_* are shown on the left, with the corresponding definitions on the detail on the right.

first, in all the available datasets, with ϕ_+ indicating transitions to higher velocities with increasing time ($\Delta U_* > 0$) and ϕ_- transitions to lower ones ($\Delta U_* < 0$).

IV. RESULTS

A. Rate of temporal transitions

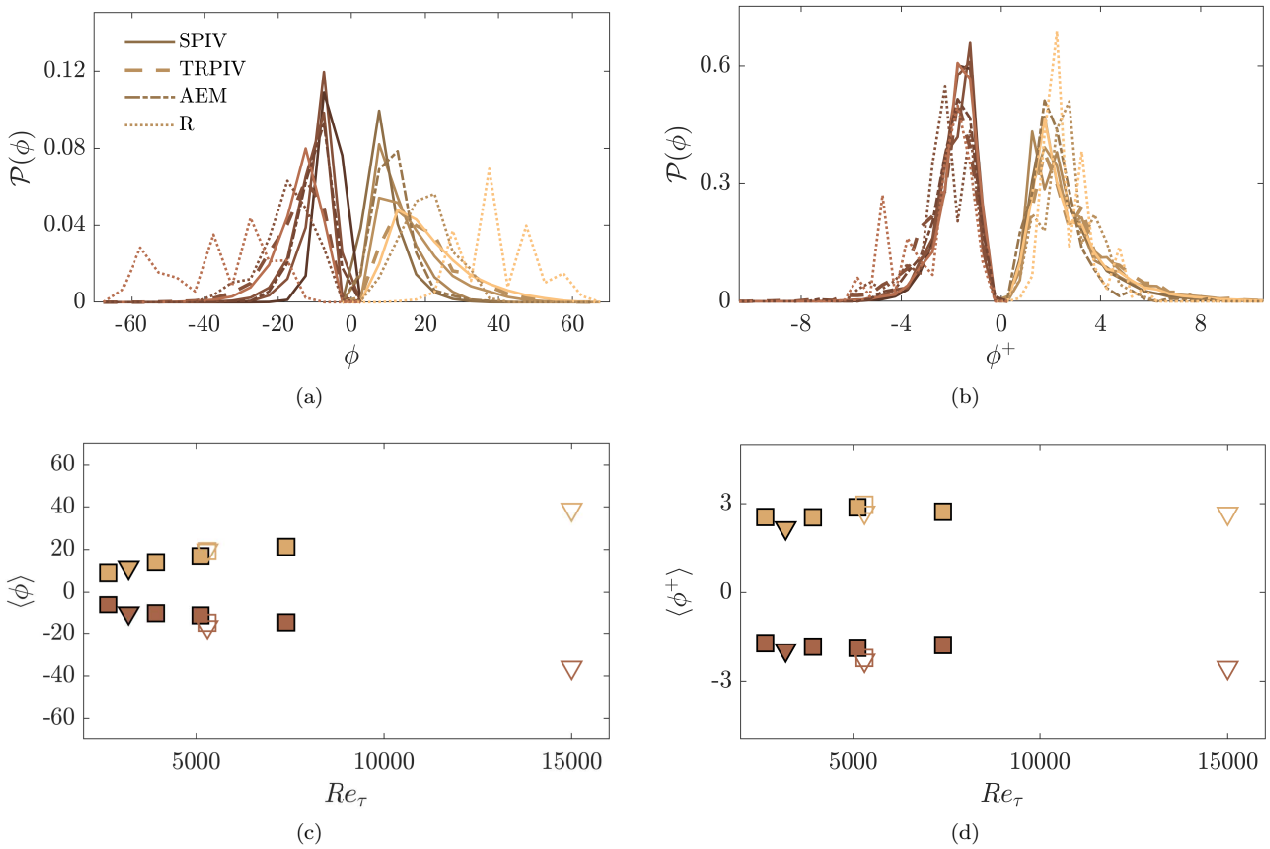

FIG. 4. Probability density function and mean values of transition angles ϕ_+ and ϕ_-, in outer (a,c) and inner (b,d) scaling ($\phi = \tan^{-1}(\Delta U_*/\Delta t)$). SPIV is denoted by ■, AEM by ▼, TRPIV by □, and R1 (R2) by ▽ (see also table I). Colors of each transition angle as in figure 3 (with lighter shades indicating increasing Re_τ).

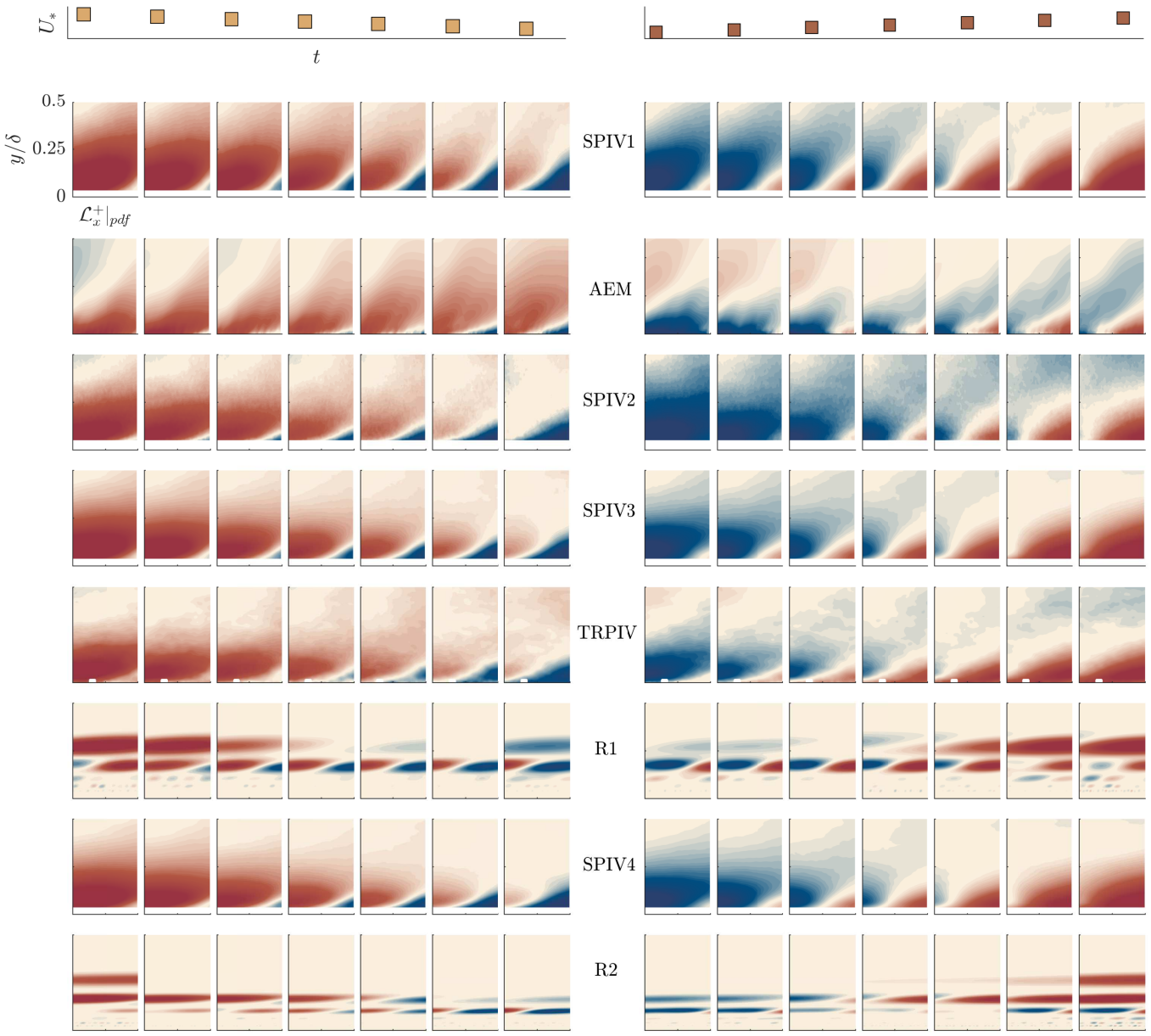

FIG. 5. Conditionally averaged streamwise velocity fluctuations in increasing Re_τ (from top to bottom) for each type of transition, $u|\phi_+$ (left) and $u|\phi_-$ (right) as shown schematically with symbols on top (in order to provide spatially continuous structures from left to right in the contour plots, time increases from right to left for the indicated transitions in U_*, following the convention from [1]).

Both the probability density function and the mean values of the transition angles exhibit fairly good collapse in inner units for all datasets, especially for ϕ_- (figures 4b and 4d), while a monotonic increase in both angles is seen with Reynolds number in outer units (figures 4a and 4c), in line with the earlier observations from the $\mathcal{P}(U,t)$ fields (figure 2). In particular, results from all experimental datasets indicate a very good collapse for both ϕ_- and ϕ_+ angles in inner units. The resolvent-based datasets (R1, R2) indicate a more discrete range of values for the transition angles (especially noticeable in the outer normalisation), due to the model's discrete scale input. On the other hand, the AEM dataset, being broadband in frequency space, allows for a fuller range of the resulting transitional angles, with only ϕ_+ being slightly underestimated due to a narrower tail of the p.d.f. (figure 4b). Overall, given the broad range of the input data used here, these metrics illustrate the robustness of the observed patterns despite these discrepancies.

It has been previously shown that the transitions in the p.d.f. of U discussed above, were associated with well-defined variations in the fluctuations, revealed through conditional averaging [1]. More precisely, ϕ^+ transitions (towards higher velocities) were shown to be associated with the passage of an inclined low-speed structure followed by a high-

speed one (figure 5, left), while the opposite was true for ϕ^- transitions (figure 5, right). Very similar behaviour in the conditionally averaged fluctuation fields was observed in the current study for all additional datasets. Regarding the experimental datasets, the use of a uniform convection velocity did not seem to affect the resulting structures in either the phase or the amplitude of the observed patterns. For similar Reynolds numbers (SPIV3, TRPIV), their inclination with respect to the horizontal as well as their vertical extent also compare very well, however they do seem to decrease with increasing Reynolds number (SPIV1, SPIV4). The p.d.f. threshold $\mathcal{P}_{th}$ has been shown to affect the wall normal location where the structures are centered and, to some degree, their vertical extent and inclination [1]; here, the same threshold is applied to all experimental datasets for consistency (see Table I), however higher p.d.f. values for lower velocities are observed in general for higher Reynolds number datasets (see figure 2). As such the choice of a constant $\mathcal{P}_{th}$ for all datasets might be partly responsible for these differences with Reynolds number. On the other hand, for modelled datasets there are much more pronounced disparities. As was already discussed in our previous work [1], the resolvent datasets are able to replicate the phase change in the conditional structures observed in experiments, however they are very localised in y due to the discrete frequency input of the model. On the contrary, the AEM, given its broadband frequency input, succeeds better in capturing a wider wall-normal extent for the conditional fluctuating fields, however the phase and, to a smaller extent, the geometry of the structures exhibit differences from all other datasets. This is intriguing, given the success of the model in statistically predicting the rate of these transitions (see figure 4). It is likely that the reason for this discrepancy lies in the lack of clearly formed patterns in the p.d.f for the AEM, where there is an almost monotonic decrease in the p.d.f values with velocity (figure 2). Tracing the transitions of $U_* = \min(U|\mathcal{P}(U,t) > \mathcal{P}_{th})$ in those cases might lead to correct overall transition rate estimates, but a mismatch in where these transitions occur in time, resulting in discrepancies when fluctuating fields are then averaged over these snapshots. Overall, the robustness of these features is clearly highlighted when assessing both snapshot and time-resolved PIV data, while the differences observed in the models appears to be mostly from their own distinct inherent limitations.

B. Temporal Coherence

As was mentioned above, the local peaks of $\mathcal{P}(U)$ are indicative of the presence of UMZs in the flow at a specific snapshot (see for example figure 1), a method that has been followed almost universally for UMZ identification and statistical analysis of their characteristics (one notable exception been the method described in [47]). When longer time (space) information is available, the resulting $\mathcal{P}(U,t)$ exhibits robust temporal patterns (figure 2) the rate of which was quantified in the first part of this section. These transitions have also been indirectly linked to the temporal variation in the number of UMZs (see the relevant discussion in [1]).

Aside from these transitions, however, time (space) information allows further analysis of UMZ characteristics more directly. In particular, visual inspection of $\mathcal{P}(U,t)$ reveals that an increase in Reynolds number in outer scaling leads to a decrease in the temporal coherence of local p.d.f. peaks (figure 2 left), an observation also reflected in the resolvent datasets. On the other hand, temporal coherence of UMZs is much less discernible in the AEM, where there is an almost monotonic decrease in the values of $\mathcal{P}(U,t)$ for decreasing velocity (especially obvious in the 3D representation of the morphology in figure 6d). The topic of temporal coherence has been partly addressed by Laskari *et al.* [16] who observed that high-speed events, linked to a low number of UMZs, exhibited longer coherence than low-speed ones, associated with multiple UMZs. In this work, we follow a more targeted approach, seeking to quantify the temporal coherence of UMZs for selected modal velocities, focusing on Reynolds number scaling and individual model performance.

In all datasets, UMZs are identified as local peaks of $\mathcal{P}(U)$ for each snapshot (see also figure 1); the detection parameters are kept the same with some appropriate adjustments made for the modelling databases, due to their bias towards velocities closer to U_∞, which lead to higher maximum p.d.f. values (also reflected in the choice of $\mathcal{P}_{th}$, table I). For a relevant discussion on this disparity see [1] and for more details on the detection thresholds see [16]. Only peaks identified in at least three consecutive snapshots ($t \sim 20^+$) are considered. The number of consecutive snapshots for which a UMZ can be detected has previously been used as an indication of temporal coherence [16]. To avoid the discrete nature of this approach, here we introduce a different metric, based on the 3D peak morphology that also exploits the available temporal information more fully. Specifically, the temporal extent, $\mathcal{T}(U_m)$, of the time-coherent UMZ at a modal velocity U_m, is defined as the time for which the peak retains at least 85% of its maximum value (see figure 7 for an illustration of the approach). The total drop-off percentage of the maximum peak value varies significantly between peaks of different datasets and can be much greater than 85%; this threshold percentage however (identical for all datasets for consistency) is chosen because all identified peaks decrease monotonically to at least 85% of their original value. As such, here, we are interested in comparing the time it takes for peaks to reach this threshold, rather than the final drop-off level of their maximum value. This definition of time coherence explicitly combines space and time information: at time t_m, a spatial extent $\mathcal{L}_x^+|_{p.d.f.} = 2000$ is used to construct $\mathcal{P}(U,t_m)$ and

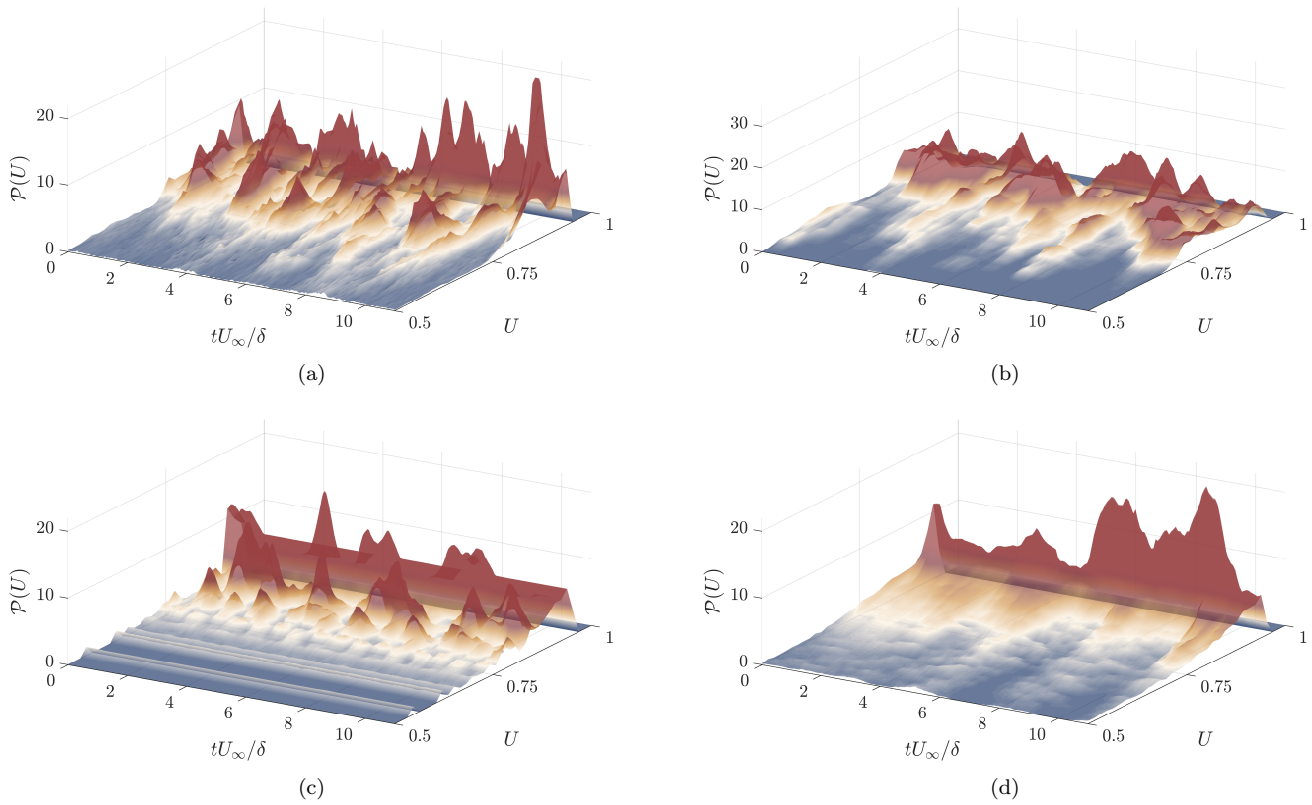

FIG. 6. 3D variation of $\mathcal{P}(U,t)$ for experimental (top) and model datasets (bottom): TRPIV (a), SPIV3 (b), R1 (c), AEM (d).

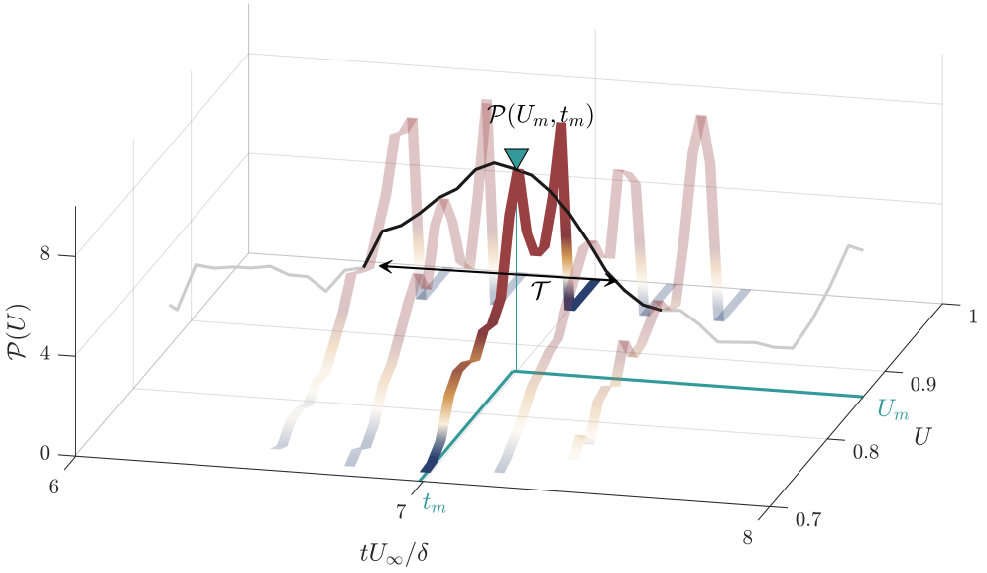

FIG. 7. Illustration of the evolution of $\mathcal{P}(U_m, t_m)$ (symbol), an instantaneous, time-coherent, UMZ peak at time t_m and modal velocity U_m, and its extent in time, $\mathcal{T}$, calculated at 85% of the peak value.

identify $\mathcal{P}(U_m, t_m)$ as a local peak at a modal velocity U_m; the peaks' extent in time, $\mathcal{T}(U_m)$, is then determined by the peak morphology in the temporal axis. It follows that statistical analysis of the temporal coherence can be performed for each modal velocity U_m, according to the binning procedure followed for the construction of $\mathcal{P}$ (see section III). To improve convergence, however, since the resulting temporal coherence does not vary significantly with U_m, the statistical analysis for $\mathcal{T}(U_m)$ is performed in bins of double the size ($0.03U_\infty$, red shaded regions in figure 8a). In what follows, we analyse the temporal coherence of modal velocity peaks belonging in three representative bins which correspond (based on the mean velocity profile) to wall-normal locations in the middle of the log-region ($3/\sqrt{Re_\tau} \leq y/\delta \leq 0.2$), as well as close to its lower and upper limits (see figure 8b). It should also be noted that for all subsequent results, a temporal filter (effective resolution of $dt^+ = 32$) was applied to all datasets. The scaling trends discussed below, remained largely unchanged; filtering mostly affected the time-resolved experimental dataset (TRPIV), for which $\mathcal{P}(U)$ was more noisy (see also figure 2) and exhibited slightly lower values of temporal coherence than all the rest. The filter size was selected such that the resulting temporal resolution would be comparable to the spatial one (see table I) and was the minimum above which the relative values of $\mathcal{T}$ between datasets remained unchanged. The conditionally averaged p.d.f. values, preceding and following the identified UMZ peaks in time indicate that for all datasets, similar to the p.d.f. transition rates, ϕ_- and ϕ_+, inner scaling is successful in collapsing the resulting peak shapes—as far as their extent in time is considered (see figure 9, right). As was mentioned earlier however, the average level of drop-off of the maximum peak value varies markedly between datasets without an apparent trend with respect to Reynolds number scaling. It is interesting to note that time-resolved datasets (TRPIV, R1, and R2) mostly exhibit higher drop-offs compared to the rest, especially for higher velocities, although the source of this behaviour is likely different for the two databases. For the synthetic datasets based on the resolvent framework (R1, R2), the higher level of drop-off in well-defined peaks can be attributed to the discrete scale input of the model: superposition of selected modes creates distinct modal peaks in an otherwise monotonically varying p.d.f. of the mean velocity. The sole exception to this trend, in the data shown here, is dataset R1 for $0.72 \leq U_m/U_\infty \leq 0.75$ (dotted lines in figures 9c and 9d); for both R1 and R2 datasets however, this velocity range is at the lower edge, above which $\mathcal{P}(U, t)$ varies significantly (see also figure 2) and as such not as indicative or statistically accurate.

This confinement of significant p.d.f. values in a limited velocity range is one of the main limitations of the two resolvent-based datasets and is also apparent in the lack of any peaks present at the lowest velocity range ($0.63 \leq U_m/U_\infty \leq 0.66$, figures 9a and 9b). On the other hand, the high average drop-off level observed in the

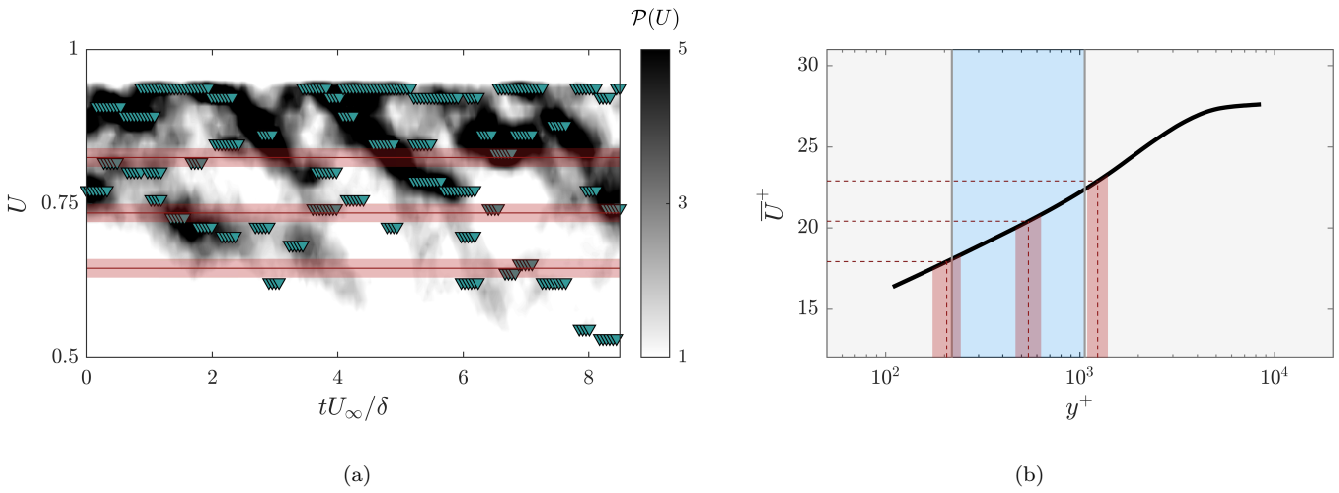

(a) (b)

FIG. 8. (a) Illustration of multiple time-coherent UMZ peaks (symbols) overlaid on $\mathcal{P}_U$. Statistics of $\mathcal{T}(U_m)$ in what follows are calculated at $0.63 \leq U_m/U_\infty \leq 0.66$, $0.72 \leq U_m/U_\infty \leq 0.75$, and $0.81 \leq U_m/U_\infty \leq 0.84$ (shaded regions). (b) Corresponding wall-normal locations for the selected velocity regions in (b), based on the mean, $\overline{U}$ (here for TRPIV). Blue shaded region indicates the logarithmic region extent ($3/\sqrt{Re_\tau} \leq y/\delta \leq 0.2$).

time-resolved experimental dataset (TRPIV) when compared to almost all other non-time resolved ones (SPIV1, SPIV2, SPIV3, SPIV4, solid lines in figure 9), regardless of Reynolds number, might be more indicative of differences due to space-time conversion—a process which was not observed to impose any significant influence on the metrics discussed up until this point. As was mentioned in section III, the time-resolved dataset did exhibit overall higher $\mathcal{P}(U)$ values compared to its snapshot counterpart at comparable Reynolds numbers (figures 2, 6a and 6b), attributed to the higher freestream noise present; however, given the normalisation of the peak magnitude here (the drop-off is quantified relative to the maximum peak value) this is not likely to influence the observed disparity between low- and high-speed datasets. Finally, the AEM dataset (dot-dash lines in figure 9) exhibits progressively worse collapse of the conditional peak shape with increasing velocity, with larger temporal coherence and very low drop-off levels, compared to the rest of the datasets.

These findings follow directly from the considerable disparity observed in the $\mathcal{P}(U,t)$ contours of the dataset (figures 2 and 6d), where the temporal patterns of the p.d.f. were broader and less prominent. The relative lack of instantaneous information in the construction of the AEM dataset (eddies randomly placed in the spatial domain) can partly explain these deviations from the experimentally observed behaviour. Another likely culprit of such discrepancies however, is the much larger number of vectors representative of higher velocities (as U_∞ is approached) relative to the other datasets, inherent in the construction of the AEM: packets of nested eddies superimposed on an otherwise irrotational freestream and inducing a corresponding superposition of velocity deficits, lead to a much denser eddy population closer to the wall than closer to the freestream. As such, the largest eddies (with the lowest velocity deficits) occupy an increasingly large proportion of the flow field which is then characterised by velocities close to U_∞ and leads to the aforementioned almost monotonic increase of $\mathcal{P}(U,t)$ with increasing velocity.

Looking more closely at the statistics of the temporal coherence, $\mathcal{T}$, the same Reynolds number scaling for inner and outer normalisation as the one observed for the conditionally averaged peak shape, is also observed here (figures 10 and 11). More specifically, the p.d.f. of $\mathcal{T}(U_m)$ for all experimental datasets and all three representative velocity regions for U_m, collapses in inner units (figure 10, right). Due to the aforementioned limitation in the two lowest velocity ranges for R1 and R2, it is only for the highest velocity band ($0.81 \leq U_m/U_\infty \leq 0.84$, figure 10f) that the two resolvent-based datasets also collapse on the experimental ones, while the lack of statistical convergence is clear for $0.72 \leq U_m/U_\infty \leq 0.75$ (figure 10d), and the lack of any peaks present at lower velocities can be seen for $0.63 \leq U_m/U_\infty \leq 0.66$ (figure 10b). On the other hand, the p.d.f of $\mathcal{T}(U_m)$ based on the AEM dataset is seen to deviate from all other datasets and for all three U_m regions, leaning towards higher values on average and a slightly more limited range overall. The latter is an interesting contrast to the broader shape of $\mathcal{P}(\mathcal{T}^+)$ for the R1 and R2 datasets (at the highest velocity range). A limited frequency content in the construction of the resolvent datasets was seen to be reflected in a limited range for the p.d.f. transitions (ϕ_+ and ϕ_-) when compared to the wider range of values from the broadband frequency content in AEM (figure 4); however the relative lack of temporal information on the latter that is inherently present in the former leads to the opposite picture emerging for the two databases in

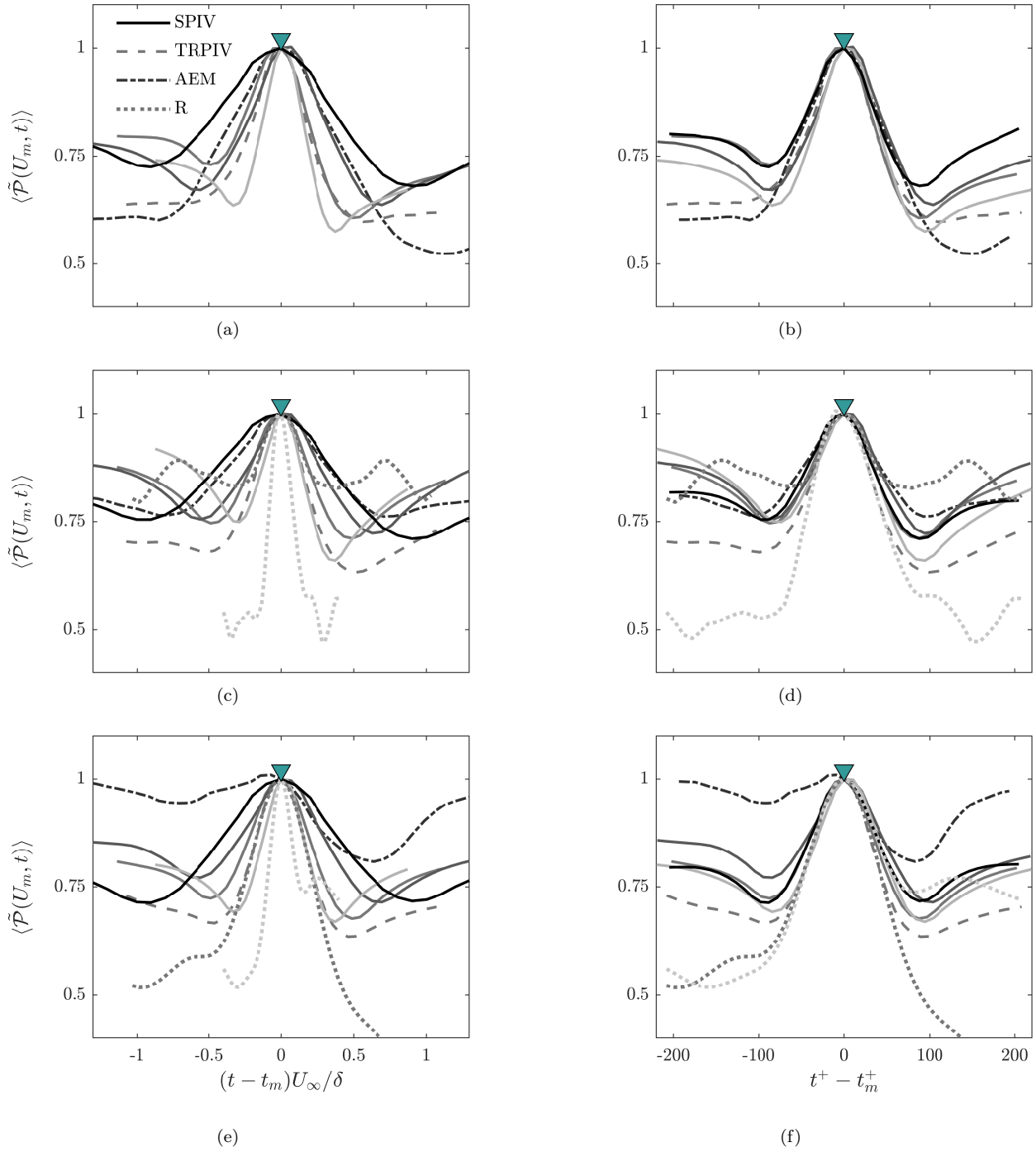

FIG. 9. Conditionally averaged p.d.f values with respect to time, $\langle\tilde{\mathcal{P}}(U_m,t)\rangle$, for all datasets, normalised with the maximum peak value, $\mathcal{P}(U_m,t_m)$. Temporal axis in outer (left) and inner (right) scaling, for $0.63 \leq U_m/U_\infty \leq 0.66$ (a, b), $0.72 \leq U_m/U_\infty \leq 0.75$ (c, d), and $0.81 \leq U_m/U_\infty \leq 0.84$ (e, f). Increasing Re_τ is denoted with lighter colours. Following figure 8a, symbols denote the UMZ peaks at $t = 0$.

the p.d.f. of temporal coherence.

These observations are further supported in the scaling of the mean values of $\mathcal{T}$ which, for most datasets, is seen to approximate a value of $\langle\mathcal{T}^+\rangle = 100 \pm 50$ (figure 11, right). Values for R1 and R2 are seen to deviate slightly from this when $0.72 \leq U_m/U_\infty \leq 0.75$ and no data is available for $0.63 \leq U_m/U_\infty \leq 0.66$. In contrast, for the AEM, agreement is only found for this lowest velocity range while higher values of $\langle\mathcal{T}^+\rangle \approx 130$ are predicted for the higher velocities. In line with the observations for $\mathcal{P}(\mathcal{T})$, Reynolds number scaling for $\mathcal{T}$ is also reflected in the standard deviation

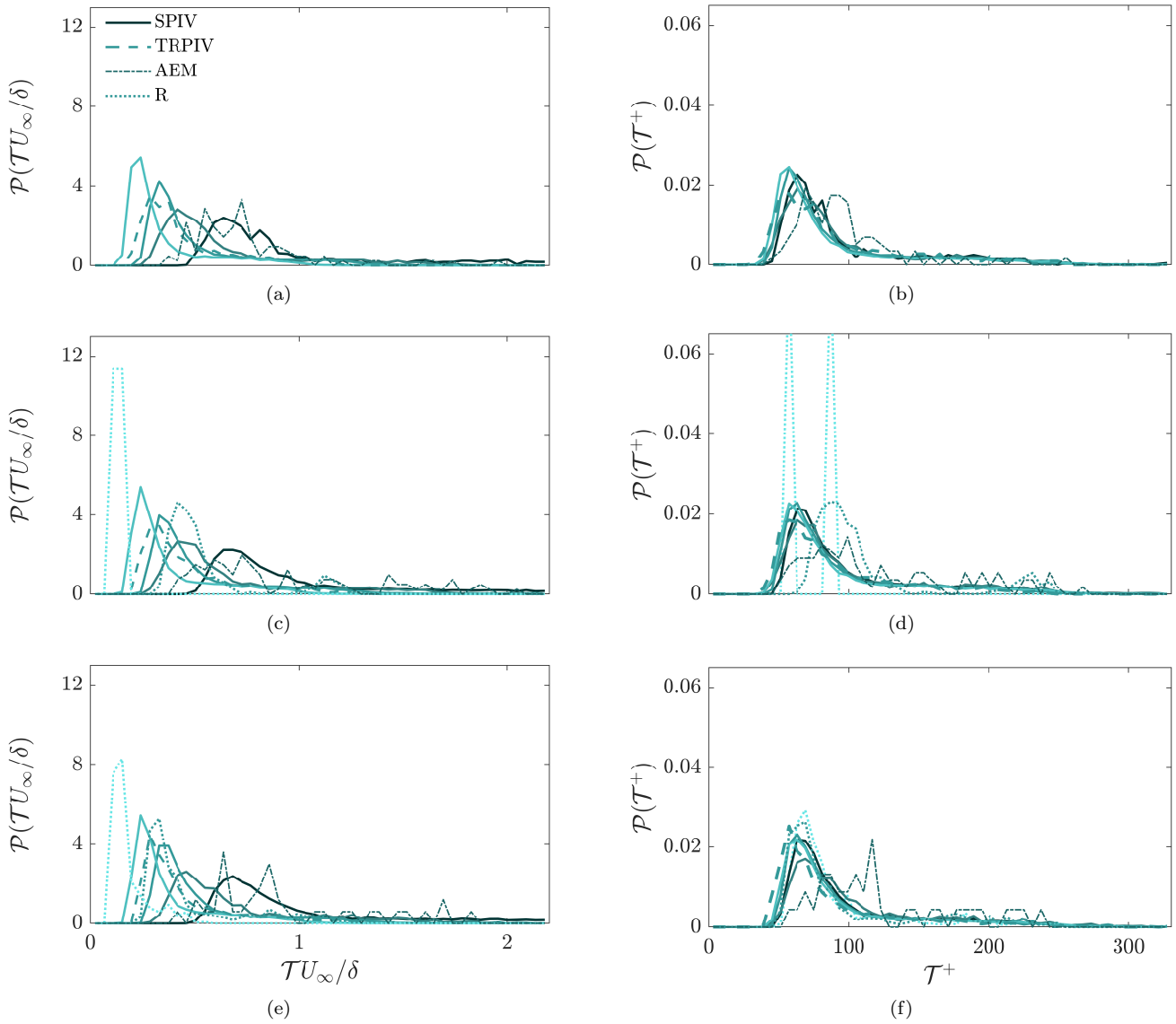

FIG. 10. Pdf of $\mathcal{T}(U_m)$, as was defined in figure 7. Outer (left) and inner (right) scaling, for $0.63 \leq U_m/U_\infty \leq 0.66$ (a, b), $0.72 \leq U_m/U_\infty \leq 0.75$ (c, d), and $0.81 \leq U_m/U_\infty \leq 0.84$ (e, f). Increasing Re_τ is denoted with lighter colours.

around the mean (error bars in figure 11), which is seen to decrease with Reynolds number in outer units (figure 11, left), while it is almost constant for all datasets ($\sim 50^+$) in inner scaling. These trends also delineate more clearly the improved predictions for R1 and R2 in the highest velocity range (indicated by a collapse with the experimental estimate of the standard deviation around $\langle\mathcal{T}\rangle$ for $0.81 \leq U_m/U_\infty \leq 0.84$). With respect to the experimental datasets it should be noted that, aside from deviations in the peak shape—and particularly the drop-off level of the maximum values discussed above (figure 9)—the use of a uniform convection velocity for the comparison between time-resolved and snapshot data was not seen to influence any of the scaling results for $\mathcal{T}$ presented here. The overall behaviour of $\langle\mathcal{T}\rangle$ with increasing U_m accentuates the discrepancies discussed above between the models, while it also indicates the slight increase of temporal coherence for higher modal velocities (figure 12; a similar observation was made by Laskari *et al.* [16]), although care should be taken when comparing the two studies, given the different definitions of temporal coherence followed in each.

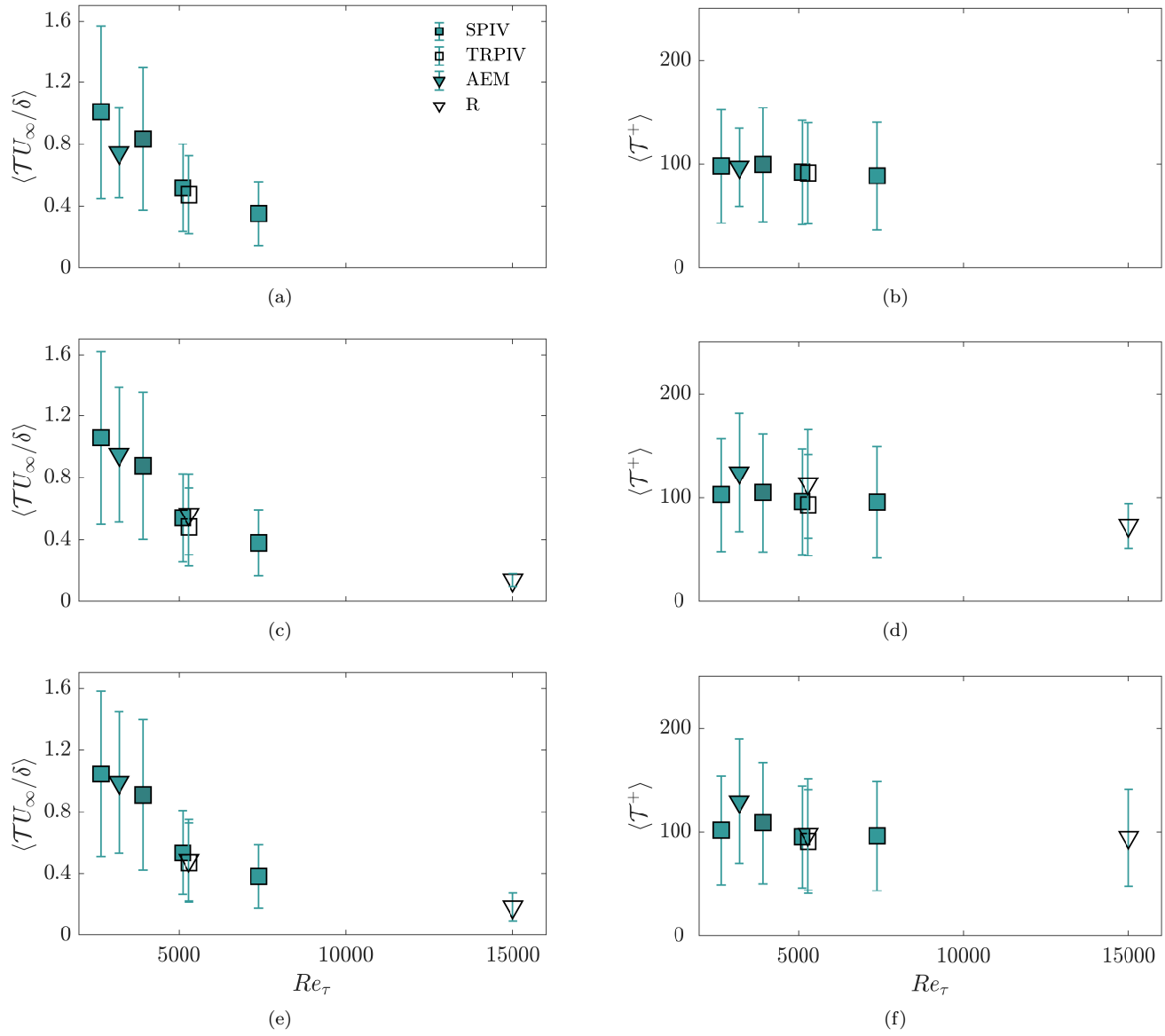

FIG. 11. Variation of $\langle \mathcal{T}(U_m) \rangle$ with Re_τ in outer (left) and inner (right) scaling, for $0.63 \leq U_m/U_\infty \leq 0.66$ (a, b), $0.72 \leq U_m/U_\infty \leq 0.75$ (c, d), and $0.81 \leq U_m/U_\infty \leq 0.84$ (e, f). Error bars equal one standard deviation.

V. SUMMARY AND DISCUSSION

From the above analysis, the robustness of the observed patterns and UMZ peak morphology in time, as well as the success of inner scaling in sufficiently collapsing most relevant metrics are the most compelling conclusions. Despite observed discrepancies, the overall agreement between datasets is notable in both mean values and distributions, especially given the variety on input data and the effort made to ensure consistency of the p.d.f. construction process and analysis.

With respect to scaling, it should be noted again here that we focus entirely on structures anchored within the logarithmic region for all the modelling datasets, where we expect specific scaling relationships based on self-similarity and we can ensure the most equitable comparison between the models. The preceding analysis on the temporal characteristics of the streamwise velocity p.d.f., including the full-scale experimental datasets, supports inner normalisation for a collapse of most metrics. While it seems that ruling out outer normalisation is certainly justifiable, it should be stressed that the range of Reynolds numbers available might not be sufficient for a definite conclusion on whether mixed scaling would be more suitable than inner scaling tested here. The highest available Reynolds number belongs to a synthetic dataset (R2), which was constructed using a particularly discrete frequency input, localised in the

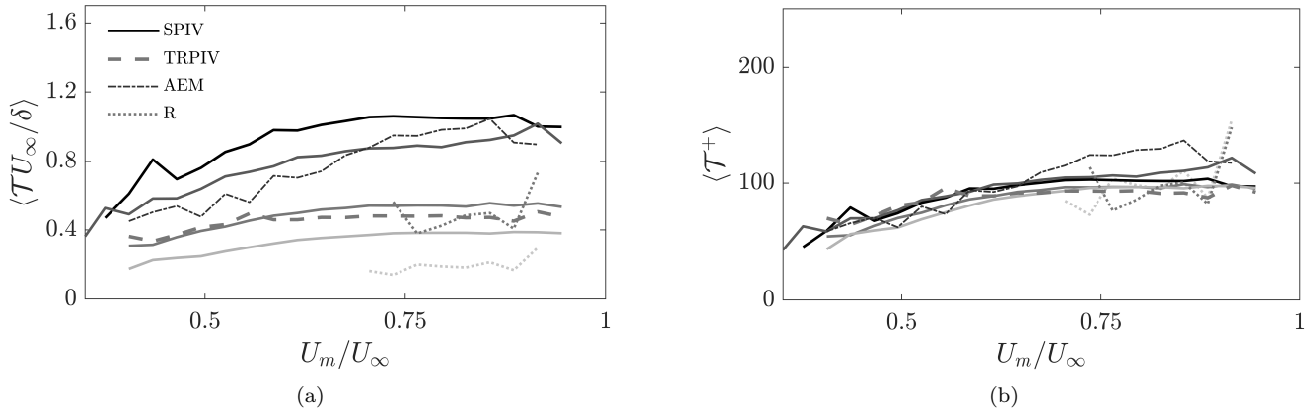

FIG. 12. Variation of $\langle \mathcal{T} \rangle$ with U_m in outer (a) and inner (b) scaling. Increasing Re_τ is denoted with lighter colours.

logarithmic region. As such, the range of Reynolds numbers in the available datasets certainly allows assessment of the two models in replicating the experimental features (and to some extent the observed scaling), however full-scale experimental datasets with a wider Reynolds number range would be required to fully assess scaling behaviour.

The experimental datasets indicated only marginal discrepancies due to the space-time conversion, even considering a uniform convection velocity in y. A higher drop-off level of the UMZ maximum peak value for the time-resolved datasets (figure 9) was the only metric where appreciable variation was observed within the different experimental databases, however, given also the lack of any clear Reynolds number scaling for this metric, more in-depth analysis would be required for further conclusions on the observed behaviour. Regarding the selection of convection velocity itself, as was mentioned in section III, a wall-normal dependence for U_c was also tested for the AEM dataset and the differences in the metrics presented here were minimal. For that particular evaluation, the p.d.f. construction process for the AEM was similar to that for the time-resolved datasets (see figure 1), with periodic boundary conditions. For consistency, all datasets were also down-sampled to match the resulting temporal resolution ($dt^+ \approx 32$) of the AEM, allowing for an additional evaluation of potential resolution effects in the trends discussed here; all effects were again shown to be inconsequential and the main trends unaltered. For completeness, different uniform convection velocities were also tested for both SPIV and AEM datasets, again with only marginal differences observed. Besides space-time conversion, the experimental databases used here (SPIV) further highlighted that a different flow geometry (channel or external boundary layer) also has negligible influence on the resulting characteristics. This observation further cements our conclusions with respect to the model datasets (outlined in the following paragraph); it is the model construction and input selection rather than the flow geometry that leads to the discrepancies between the resolvent (channel) and the AEM (TBL) datasets.

Finally, with respect to model comparisons, different benefits and drawbacks of each were displayed, although the resulting conclusions presented herein apply exclusively on reproducing the temporal characteristics of $\mathcal{P}(U,t)$ and are not necessarily representative of global model performance. Synthetic datasets based on the resolvent framework have been shown to successfully replicate the characteristics of the p.d.f. transitions [1]. In the present study these findings were extended to show that for modal velocities at the outer edge of the log region, the resulting temporal coherence of UMZ peaks and Reynolds number scaling was also in good agreement with the experimentally observed behaviours. On the other hand, these datasets were limited by the discrete frequency input, inherent in the model construction, reflected in a restriction of p.d.f patterns within a narrow range of velocities (see for example figure 2) and a resulting sparser value distribution for the transition rates ϕ_- and ϕ^+ (figure 4a) and a shorter wall-normal extent in the conditionally averaged fluctuations (figure 5); temporal coherence of UMZ peaks also quickly deteriorated for velocities closer to the wall and very close to the freestream (figure 12). Regarding the synthetic dataset based on the AEM, the broadband frequency input of the model allowed a much broader range of velocities with substantial p.d.f. activity compared to the resolvent datasets, reflected in the smoother distribution of transition rates ϕ_- and ϕ^+ and the wider wall-normal extent of the conditionally averaged fluctuating velocity. However, the instantaneous structure details encompassed in the AEM also resulted in significant discrepancies in the temporal behaviour of the model when compared to experimental data, with respect to both the phase and the geometry of the conditional structures (figure 5), which could be traced back to a much less prominent peak behaviour in $\mathcal{P}(U,t)$ (figures 2 and 6d), with p.d.f. values almost monotonically decreasing with decreasing velocity. This was also reflected in the disparities observed in the temporal coherence of the UMZ peaks for the AEM, which was shown to be larger on average and with a more discrete distribution of values than either the experimental or the resolvent-based datasets. Aside from the lack of a well-defined instantaneous structure, another potential explanation for the observed discrepancies in the AEM is an

increase in the number of vectors belonging to higher velocities: the largest eddies of the nested packets occupy a much larger proportion of the flow field, averaging out larger velocity deficits from smaller eddies which have a more limited wall-normal extent.

VI. CONCLUSIONS

The temporal characteristics of the p.d.f. of the streamwise velocity were evaluated in a variety of experimental and synthetic datasets of wall-bounded flows, the latter based on the attached eddy model (AEM, [3]) and the resolvent framework [2]. The effects of Reynolds number, availability of temporal information, and specifics of model construction, were assessed. The temporal patterns in $\mathcal{P}(U,t)$, first analysed by Laskari and McKeon [1], were seen to be robust and repeatable in all datasets. The rate of transitions, ϕ, and the temporal coherence of UMZ peaks are both found to scale in inner units. The use of a uniform convection velocity in space-to-time transformations as well as the specific flow geometry (internal vs external) both had a negligible effect in most metrics analysed here. Overall, the two synthetic datasets were able to replicate many of the experimentally observed behaviours, with a narrow frequency input and lack of instantaneous structural details being the main drawbacks for the resolvent and AEM based datasets, respectively.

ACKNOWLEDGMENTS

The support of ONR through Grant No N00014-17-1-3022 (AL, BJM) is gratefully acknowledged.

[1] A. Laskari and B. J. McKeon, Temporal characteristics of the probability density function of velocity in wall-bounded turbulent flows, J. Fluid Mech. **913**, A6 (2021).
[2] B. J. McKeon and A. S. Sharma, A critical-layer framework for turbulent pipe flow, J. Fluid Mech. **658**, 336 (2010).
[3] A. E. Perry and M. S. Chong, On the mechanism of wall turbulence, J. Fluid Mech. **119**, 173 (1982).
[4] C. D. Meinhart and R. J. Adrian, On the existence of uniform momentum zones in a turbulent boundary layer, Phys. Fluids **7**, 694 (1995).
[5] R. J. Adrian, C. D. Meinhart, and C. Tomkins, Vortex organization in the outer region of the turbulent boundary layer, J. Fluid Mech. **422**, 1 (2000).
[6] J. Eisma, J. Westerweel, G. Ooms, and G. E. Elsinga, Interfaces and internal layers in a turbulent boundary layer, Phys. Fluids **27**, 055103 (2015).
[7] C. M. de Silva, J. Philip, N. Hutchins, and I. Marusic, Interfaces of uniform momentum zones in turbulent boundary layers, J. Fluid Mech. **820**, 451 (2017).
[8] B. J. Balakumar and R. J. Adrian, Large- and very-large-scale motions in channel and boundary-layer flows, Philos. Trans. R. Soc. A **365**, 665 (2007).
[9] N. Hutchins and I. Marusic, Evidence of very long meandering features in the logarithmic region of turbulent boundary layers, J. Fluid Mech. **579**, 1 (2007).
[10] M. Guala, S. E. Hommema, and R. J. Adrian, Large-scale and very-large-scale motions in turbulent pipe flow, J. Fluid Mech. **554**, 521 (2006).
[11] J. P. Monty, N. Hutchins, H. C. H. Ng, I. Marusic, and M. S. Chong, A comparison of turbulent pipe, channel and boundary layer flows, J. Fluid Mech. **632**, 431 (2009).
[12] W. Li, D. Roggenkamp, V. Paakkari, M. Klaas, J. Soria, and W. Schröder, Analysis of a drag reduced flat plate turbulent boundary layer via uniform momentum zones, Aerosp. Sci. Technol. **96**, 105552 (2019).
[13] Y. Farsiani, Z. Saeed, B. Jayaraman, and B. Elbing, Modification of turbulent boundary layer coherent structures with drag reducing polymer solution, Phys. Fluids **32**, 015107 (2020).
[14] C. M. de Silva, N. Hutchins, and I. Marusic, Uniform momentum zones in turbulent boundary layers, J. Fluid Mech. **786**, 309 (2016).
[15] T. Saxton-Fox and B. J. McKeon, Coherent structures, uniform momentum zones and the streamwise energy spectrum in wall-bounded turbulent flows, J. Fluid Mech. **826**, R6 (2017).
[16] A. Laskari, R. de Kat, R. J. Hearst, and B. Ganapathisubramani, Time evolution of uniform momentum zones in a turbulent boundary layer, J. Fluid Mech. **842**, 554 (2018).
[17] K. Wang, L. Biahui, and L. Liu, Experimental measurement of coherent structures in turbulent boundary layers using moving time-resolved particle image velocimetry, Phys. Fluids **32**, 115102 (2020).
[18] M. Heisel, C. M. De Silva, N. Hutchins, I. Marusic, and M. Guala, On the mixing length eddies and logarithmic mean velocity profile in wall turbulence, J. Fluid Mech. **887**, R1 (2020).

[19] R. J. Hearst, C. M. de Silva, E. Dogan, and B. Ganapathisubramani, Uniform-momentum zones in a turbulent boundary layer subjected to freestream turbulence, J. Fluid Mech. **915**, A109 (2021).

[20] M. Bross, T. Fuchs, and C. J. Kähler, Interaction of coherent flow structures in adverse pressure gradient turbulent boundary layers, J. Fluid Mech. **873**, 287 (2019).

[21] A. Thavamani, C. Cuvier, C. Willert, J. M. Foucaut, C. Atkinson, and J. Soria, Characterisation of uniform momentum zones in adverse pressure gradient turbulent boundary layers, Exp. Therm. Fluid Sci. **115**, 110080 (2020).

[22] O. J. Williams, D. Sahoo, M. L. Baumgartner, and A. J. Smits, Experiments on the structure and scaling of hypersonic turbulent boundary layers, J. Fluid Mech. **834**, 237 (2017).

[23] M. Gul, G. E. Elsinga, and J. Westerweel, Internal shear layers and edges of uniform momentum zones in a turbulent pipe flow, J. Fluid Mech. **901**, A10 (2020).

[24] S. C. Morris, S. R. Stolpa, P. E. Slaboch, and J. C. Klewicki, Near-surface particle image velocimetry measurements in a transitionally rough-wall atmospheric boundary layer, J. Fluid Mech. **580**, 319 (2007).

[25] M. Heisel, T. Dasari, Y. Liu, J. Hong, F. Coletti, and M. Guala, The spatial structure of the logarithmic region in very-high-Reynolds-number rough wall turbulent boundary layers, J. Fluid Mech. **857**, 704 (2018).

[26] S. Senthil, C. Atkinson, and J. Soria, Analysis of the spanwise extent and time persistence of uniform momentum zones in zero pressure gradient and adverse pressure gradient turbulent boundary layers, J. Phys. Conf. Ser. **1522**, 012013 (2020).

[27] X. Chen, Y. M. Chung, and M. Wan, Uniform-momentum zones in a turbulent pipe flow, J. Fluid Mech. **884**, A25 (2020).

[28] X. Chen, Y. M. Chung, and M. Wan, The uniform-momentum zones and internal shear layers in turbulent pipe flows at $r$eynolds numbers up to $re_\tau = 1000$, Int. J. Heat Fluid Flow **90**, 108817 (2021).

[29] G. Taylor, The spectrum of turbulence, Proc. R. Soc. Lond. A. **164**, 476 (1938).

[30] J. C. C. Bautista, A. Ebadi, C. M. White, G. P. Chini, and J. C. Klewicki, A uniform momentum zone-vortical fissure model of the turbulent boudnary layer, J. Fluid Mech. **858**, 609 (2019).

[31] F. Eich, C. M. de Silva, I. Marusic, and C. J. Kähler, Towards an improved spatial representation of a boundary layer from the attached eddy model, Phys. Rev. Fluids **5**, 034601 (2020).

[32] A. S. Sharma and B. J. McKeon, On coherent structure in wall turbulence, J. Fluid Mech. **728**, 196 (2013).

[33] G. P. Chini, B. Montemuro, C. M. White, and J. Clewicki, A self-sustaining process model of inertial layer dynamics in high reynolds number turbulent wall flows, Phil. Trans. R. Soc. A **820**, 20160090 (2017).

[34] B. Montemuro, C. M. White, J. Clewicki, and G. P. Chini, A self-sustaining process model of inertial layer dynamics in high reynolds number turbulent wall flows, Phil. Trans. R. Soc. A **901**, A28 (2017).

[35] B. J. McKeon, Self-similar hierarchies and attached eddies, Phys. Rev. Fluids **4**, 082601 (2019).

[36] C. M. de Silva, D. T. Squire, N. Hutchins, and I. Marusic, Towards capturing large scale coherent structures in boundary layers using particle image velocimetry, in *Proceedings of the 7th Australian Conference on Laser Diagnostics in Fluid Mechanics and Combustion, Melbourne, Australia* (2015).

[37] F. H. Clauser, Turbulent boundary layers in adverse pressure gradients, J. Aero Sci. **21**, 91 (1954).

[38] K. A. Chauhan, P. A. Monkewitz, and H. M. Nagib, Criteria for assessing experiments in zero pressure gradient boundary layers, Fluid Dyn. Res. **41**, 021404 (2009).

[39] Y. S. Kwon, J. Philip, C. M. de Silva, N. Hutchins, and J. P. Monty, The quiescent core of turbulent channel flow, J. Fluid Mech. **751**, 228 (2014).

[40] C. M. de Silva, E. P. Gnanamanickam, C. Atkinson, N. A. Buchmann, N. Hutchins, J. Soria, and I. Marusic, High spatial range velocity measurements in a high reynolds number turbulent boundary layer, Phys. Fluids **26**, 025117 (2014).

[41] B. J. McKeon, The engine behind (wall) turbulence: perspectives on scale interactions, J. Fluid Mech. **817**, P1 (2017).

[42] I. Marusic, J. P. Monty, M. Hultmark, and A. J. Smits, On the logarithmic region in wall turbulence, J. Fluid Mech. **716**, R3 (2013).

[43] R. Moarref, A. S. Sharma, T. J. A., and B. J. McKeon, Model-based scaling of the streamwise energy density in high-Reynolds-number turbulent channels, J. Fluid Mech. **734**, 275 (2013).

[44] J. D. Woodcock and I. Marusic, The statistical behaviour of attached eddies, Phys. Fluids **27**, 015104 (2015).

[45] K. B. M. Q. Zaman and A. K. M. F. Hussain, Taylor hypothesis and large-scale coherent structures, J. Fluid Mech. **112**, 379 (1981).

[46] K. Chauhan, J. Philip, C. C. M. de Silva, N. Hutchins, and I. Marusic, The turbulent/non-turbulent interface and entrainment in a boundary layer, J. Fluid Mech. **742**, 119 (2014).

[47] D. Fan, J. Xu, M. X. Yao, and J.-P. Hickey, On the detection of internal interfacial layers in turbulent flows, J. Fluid Mech. **872**, 198 (2019).